Phonons and related spectra in bulk and monolayer V_2O_5

Churna Bhandari* and Walter R. L. Lambrecht
Department of Physics, Case Western Reserve University, Cleveland, Ohio 44106, USA
(Received 24 October 2013; published 9 January 2014; corrected 6 June 2014)

The phonons at the zone center are calculated for the layered material V_2O_5 using density functional perturbation theory and are compared with experimental infrared and Raman spectra from literature. We find that significantly better agreement is obtained when the pseudopotential treats vanadium semicore states $3s$ and $3p$ as bands. Remaining discrepancies are shown to be related to the local density approximation overestimate of the bond-stretch mode frequencies. The vibrational mode patterns are studied and presented in detail. The same method is then applied to well-separated monolayers. We find significant changes in some phonon frequencies. In particular, the highest-frequency vanadium vanadyl-oxygen stretch modes show a blue-shift of order 6%–8%. The origin of this blue-shift is analyzed in terms of the force-constant changes between bulk and monolayer and is found to arise from a delicate balance of short- and long-range dipolar force components. The latter are affected by the changes in dielectric constants and in the Born-effective charges. The red-shifts of some of the low-frequency modes are found also to be related to a reduction in force constants within the layer, rather than the removal of interlayer bonds. In this case, it is primarily motions along the x direction that are affected. The static and high-frequency dielectric constants are both found to be reduced in the monolayer.

DOI: 10.1103/PhysRevB.89.045109 PACS number(s): 63.20.dk, 63.22.Np, 78.30.Hv, 71.15.Mb

I. INTRODUCTION

Vanadium forms a series of oxides with different O to V ratio from VO, V_2O_3, VO_2 to V_2O_5. V_2O_3 [1,2] and VO_2 [3,4] have received much attention because of the strongly correlated nature of the d electrons and the associated metal-insulator transitions. At first sight, V_2O_5 may seem less interesting because V is in its highest oxidation state V^{5+} and thus one expects simply a wide gap insulator. However, the layered crystal structure of V_2O_5, in which one of the oxygens is singly bonded to V, means that this so-called vanadyl oxygen can easily leave the structure and lead to slightly substoichiometric oxide forms [5–7] such as V_4O_9, V_6O_{13}, and leads to interesting catalytic activity. Furthermore, as we will see in the following, the structure has also one-dimensional aspects since it consists of double V-O chains in one direction which are less strongly bound by bridge oxygens in the direction perpendicular to the chains. This leads to a band structure with a split-off conduction band with almost one-dimensional (1D) dispersion [8,9]. Either oxygen vacancies or intercalated alkali-metal ions can dope this band and lead to interesting properties in the so-called V_2O_5 bronzes such as $Li_xV_2O_5$ which have received significant attention for their magnetic properties [10]. Aside from the crystalline form, V_2O_5 also exists in various nanoforms in which layers are rolled up in tubes, much like carbon nanotubes [11,12], or they can form thin nanofibers [13,14], nanowires [15], or even nanoflowers [16].

Thus, not surprisingly, V_2O_5 has been extensively studied and found various types of applications. For example, it can be used as a window for solar cells and antireflection coatings [17]. It has also very useful mechanical properties, for instance, Gu *et al.* [18] have shown that sheets made of entangled vanadium oxide nanofibers behave like actuators (artificial muscles) that contract reversibly under an electrical signal. It also exhibits excellent multicolor electrochromic behavior [17,19] in electrochemical reactions. It can be used as the critical temperature sensors [20] and light detectors. One of its main uses is as a catalyst in various oxidation reactions of hydrocarbons and sulfur dioxide. The possibility of intercalation of the layered structure is also attractive for Li batteries [21].

Our main motivation for this study is that with the development of exfoliation techniques for graphene and other two-dimensional (2D) materials, it should be possible to obtain monolayer or few layer V_2O_5. Ultrathin nanowires have already been reported by Kim *et al.* [14]. It is therefore of interest to study how the properties of monolayer V_2O_5 differ from the bulk. Furthermore, the monolayer could potentially be further changed by injecting electrons in the conduction band through a gate bias. As a first step toward a better understanding of monolayer V_2O_5, we here study the phonon spectra of bulk and monolayer V_2O_5.

Although there have been several previous studies [22–28] of the vibrational modes of V_2O_5, there remain significant discrepancies in the literature between different calculations and between theory and experiment. A full understanding of the vibrational modes and the associated spectra is not yet available. Furthermore, while there have been some studies of surface modes using low-energy electron loss spectroscopy [29], there is no information on the phonons in monolayers. In other monolayer materials, such as MoS_2, interesting differences have been found between monolayer and bulk vibrational modes [30].

While previous comparisons between theory and experiment focused mainly on the mode frequencies alone, we prefer here to compare directly with the measured experimental spectra by calculating the infrared and Raman spectra. Previous experimental studies were accompanied by phenomenological force-field calculations to extract the vibrational mode frequencies. We prefer, however, to compare directly with the data. For example, we compare directly with the the reflectance measurement carried out by Clauws *et al.* [24,26] for the

*churna.bhandari@case.edu

infrared modes. We also perform calculations of the Raman tensors which allow us to compare not only the frequencies of the Raman-active modes, but also their intensities with the experimental data of Clauws *et al.* [26]. The paper is organized as follows. In Sec. II, we briefly summarize the structure details of V_2O_5. In Sec. III, we present the computational details. Finally, in Sec. IV we will present and discuss our results for both bulk and monolayer.

II. STRUCTURE DETAILS V_2O_5

V_2O_5 is an orthorhombic crystal with space group $Pmmn$ or D_{2h}^{13}. The unit cell contains two formula units of V_2O_5. There are three structurally inequivalent oxygen atoms, which are called vanadyl-oxygen, bridge oxygen, and chain oxygen, which are respectively bonded to 1, 2, and 3 vanadium atoms while each vanadium is coordinated with five oxygen atoms. A sixth oxygen atom in the next layer completes a distorted octahedron but is much farther away, leading to a layered structure. The vanadium atoms, vanadyl-oxygen, and chain oxygens occupy $4f$ Wyckoff position with C_s symmetry, the bridge oxygens are in $2a$ Wyckoff positions with site symmetry C_{2v}. In total, there are four vanadium atoms, four vanadyl-oxygen which lie directly on top (or below) the vanadium atoms, four chain oxygen, and two bridge oxygen atoms in the unit cell. It has a layered structure which is formed by a stacking of weakly interacting layers. Figures 1(a) and 1(b) show the schematic diagram of V_2O_5 as seen from side and top, respectively. The lattice parameters of V_2O_5 are $a = 11.51$ Å, $b = 3.56$ Å, and $c = 4.37$ Å for bulk [31]. The b direction corresponds to the chains, and the c direction is perpendicular to the layers. A monolayer structure is modeled by increasing the distance between the layers along the c axis.

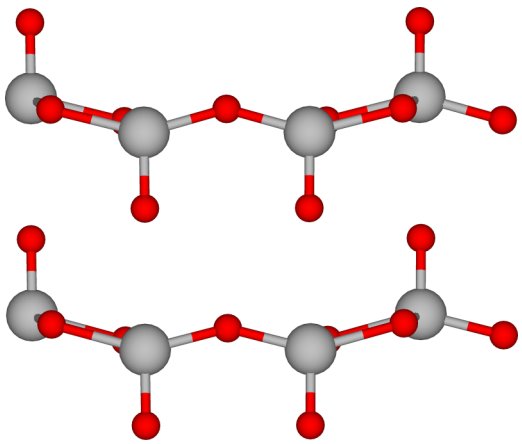

(a)

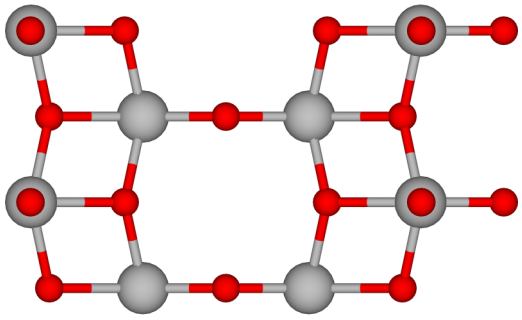

(b)

FIG. 1. (Color online) Crystal structure of bulk V_2O_5: (a) side view and and (b) top view; the red balls are oxygen and the blue balls are vanadium atoms.

III. METHODOLOGY

To study the vibrational properties of V_2O_5, we use the density functional perturbation method together with a plane-wave pseudopotential band-structure method as implemented in the ABINIT package [32,33], a common project of the Université Catholique de Louvain, Corning Incorporated, and other contributors (http://www.abinit.org). In the linear response function calculation, the iterative minimization of the ground-state total energy [34] is followed by a calculation of the first-order perturbation of the wave functions for various perturbations: displacements of each of the atoms in all three Cartesian directions as well as the response to a static electric field in each direction. The latter is necessary to obtain the long-range forces responsible for the longitudinal optical–transverse optical (LO–TO) splitting of the modes at the zone center. We here focus only on the modes at Γ as they are the ones directly observable in Raman scattering and infrared measurements. Effectively, one calculates the second-order derivatives of the total energy with respect to atomic displacements [35] using density functional perturbation theory (DFPT), which gives the force constants or dynamical matrix. It also allows us to obtain the second derivative with respect to the electric field which gives the dielectric tensor and the mixed derivatives which give the Born-effective charges. As a consequence, one can get the long-range LO/TO splitting of infrared modes at $q = 0$. According to the $2n + 1$ theorem [36], the perturbation in wave function correct up to n-th order gives the correction in total energy up to $2n + 1$ order. Thus, one can obtain the third derivatives of the total energy with respect to an atomic displacement and twice with respect to the electric field which allows us to calculate the Raman tensor $\delta\chi_{\alpha\beta}/\delta\tau$, where τ is an atomic position vector. From the Born-effective charges and the eigenvectors, one can obtain the oscillator strength and, thus, we can fully model the infrared spectra. The only parameter we do not calculate explicitly is the lifetime or damping constant.

Both the DFPT and initial structural relaxation with density functional theory (DFT) are all carried out in the plane-wave pseudopotential approach. This means the calculations are restricted to the valence electrons and the core-valence interactions are described by a pseudopotential. The local density approximation (LDA) for the exchange-correlation functional of type Perdew-Wang 92 LSD fit to Ceperley-Alder [37] was used. We have used two different pseudopotentials both of norm-conserving LDA type. We first worked with nonrelativistic Fritz-Haber Institute (FHI) type pseudopotential using the LDA Ceperley/Alder [37] parametrization. This pseudopotential has the advantage of being rather smooth from a computational point of view. This pseudopotential had been previously

used in literature on V_2O_5 and we obtained excellent agreement with this previous study [28]. However, we found significant disagreements with experiment with this pseudopotential. Therefore, we investigated also the relativistic separable dual-space Gaussian-type Hartwigsen-Goedecker-Hutter (HGH) pseudopotentials [38]. These differ in the important aspect that the semicore states of V are treated as bands.

Total-energy convergence tests were done for both pseudopotentials. We fixed the plane-wave cutoff energy to 80 hartree which was sufficient for the total-energy convergence to within 10^{-3} hartree while going from cutoff energy from 60 to 80 hartree. For the HGH pseudopotential, a cutoff larger than 80 hartree was needed for the good convergence of the phonon frequency. For the FHI pseudopotential, a cutoff larger than 60 hartree was sufficient for the phonons. We found that there was about a 1% to 2% change in calculated frequency with cutoff 80 and 100 hartree for the HGH pseudopotential. We also checked the **k**-point convergence by taking several choices. The ratios of the unit-cell dimensions suggest that the number of divisions in the a direction of the Brillouin zone can be taken 2–3 times smaller than in the b and c directions. For the HGH pseudopotential which is rather demanding, we used a $3 \times 6 \times 6$ mesh. For the Troullier-Martins potential, we used a larger mesh so that both are well converged. Ionic positions within the unit cell were relaxed using the Broyden-Fletcher-Goldfarb-Shanno (BFGS) minimization, modified to take into account the total energy as well as the gradients [39]. We did not separately relax the lattice constants but instead kept them fixed to the experimental values for both types of pseudopotential. This avoids the LDA underestimate of the unit-cell volume. The forces were well converged within 10^{-6} hartree/bohrs root-mean-square error using the BFGS method. This is quite important especially for the third-order derivative (Raman tensor) calculations.

For the monolayer, we first varied the interlayer distance along the c axis and checked convergence with respect to the total energy. We found that a lattice constant along the c axis greater than 10 Å was sufficient to model well-separated monolayers. In this work, we chose $c = 10.58$ Å and other a and b were kept the same as bulk. For the monolayer, we used a similar k-point mesh as for the bulk but with only one division in the c direction normal to the layers. The same total-energy cutoff of 80 hartree was used for both cases. Then, the ionic positions were relaxed keeping the lattice constant unchanged.

IV. RESULTS AND DISCUSSION

A. Symmetry analysis

According to group theory analysis, V_2O_5 belongs to the D_{2h} point group. There are 14 atoms per unit cell and $3N = 42$ degrees of freedom corresponding to the zone-center modes. Among these, 3 are just translation (zero frequencies), the remaining 39 are vibrational modes (optical). The D_{2h} group at Γ, $k = 0$, has the following normal modes (irreducible representations):

$$\Gamma = 3A_u + 6B_{1u} + 3B_{2u} + 6B_{3u} + 7A_{1g} + 3B_{1g} + 7B_{2g} + 4B_{3g}.$$

We see that there are three A_{1u} modes which are silent. These modes can not be detected experimentally with light scattering or absorption. There are 15 infrared active modes, specifically $6B_{1u}$, $3B_{2u}$, and $6B_{3u}$ which are active for $E\|a$, $E\|b$, and $E\|c$, respectively. The remaining 21 modes are Raman-active modes. Because the point group includes an inversion center, only odd symmetry modes are infrared active and only even modes are Raman active. We also note that because there is an ordinary mirror-plane perpendicular to the y axis, the normal modes contain either only y displacements if they are odd with respect to this mirror plane, i.e., $A_{1u}, B_{1g}, B_{2u}, B_{3g}$ or only x and z displacements, if they are even with respect to this mirror plane, i.e., $A_{1g}, B_{1u}, B_{2g}, B_{3u}$.

B. Infrared-active modes

A comparison with previously reported infrared-active modes is not entirely trivial. Infrared spectra reflectance spectra were reported by Bootz *et al.* [23], Gilson *et al.* [22], Clauws *et al.* [24,26], and generally agree fairly well with each other. Gilson *et al.* [22], however, reported the frequencies of the maxima in reflectance, Clauws *et al.* [26] report both the TO and LO frequencies extracted from the reflectance using Kramers-Kronig analysis, Abello *et al.* [25] report polycrystalline powder transmission spectra in various hosts. That means in the latter experiment, the modes can not be assigned clearly to a specific symmetry. We also note that the transmission is given by $T = I/I_0 = e^{-\alpha d} \approx 1 - \alpha d$ with the d the thickness of the layer and α the absorption coefficient

$$\alpha(\omega) = \frac{\omega \varepsilon_2(\omega)}{cn(\omega)} \tag{1}$$

with $\varepsilon_2(\omega)$ the imaginary part of the dielectric function and $n(\omega)$ the real part of the index of refraction. Because $n(\omega)$ may have minima at the zeros of the real part $\varepsilon_1(\omega)$, where the LO modes occur, α may show features at the LO modes in addition to the TO modes which correspond to the peaks in $\varepsilon_2(\omega)$. For a typical mode, the reflectance shows a Reststrahlen band between the TO and LO modes and the peak of such bands thus lies somewhere in-between the two. For the weak modes with small oscillator strength, the TO–LO splitting is small and giving the frequency of the reflection maximum makes sense. But, for the stronger modes, it is preferable to look separately at the TO onset and LO decrease of the reflectivity.

The most direct comparison with the data can be done by calculating the reflectance directly from the dielectric function. We obtained the reflectivity from the real and imaginary parts of the dielectric tensor. The dielectric tensor is given by

$$\epsilon_{\alpha\alpha}(\omega) = \epsilon^{\infty}_{\alpha\alpha} + \frac{4\pi}{\Omega} \sum_n \frac{S_{n,\alpha\alpha}}{\omega_n^2 - \omega^2 - i\Gamma_n \omega}, \tag{2}$$

where $\epsilon^{\infty}_{\alpha\alpha}$ is the high-frequency dielectric constant, ω_n the mode frequency, ω the frequency, $S_{n,\alpha\alpha}$ the oscillator strength, Γ_n the damping parameter, and n is the mode number. The only parameter here we do not calculate directly is the damping parameter. We use the experimental values for it as given by the fit of Clauws *et al.* [26]. Figure 2 shows the comparison of our calculated reflectivity of B_{1u}, B_{2u}, and B_{3u} modes, respectively, from top to bottom with the experimental results [24]. We see that the positions of the bands and their qualitative

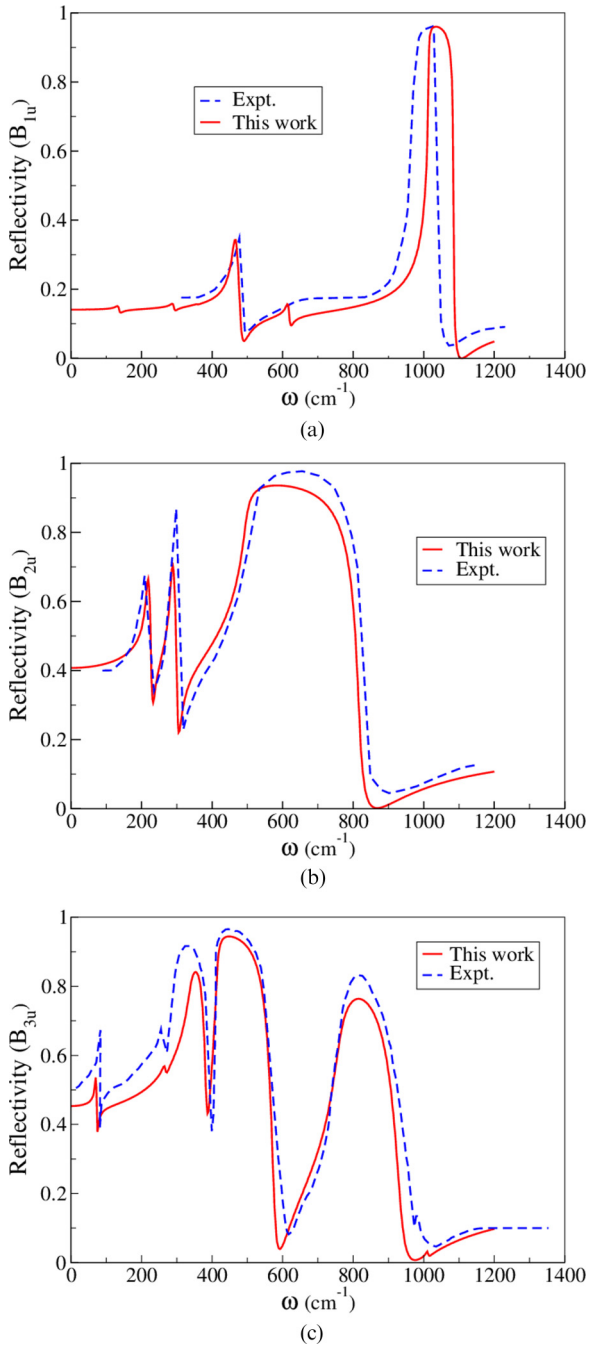

FIG. 2. (Color online) Reflectivity of IR modes vs frequency (cm^{-1}) V_2O_5.

shape are in excellent agreement with the experiment. This indicates that our calculations not only give the TO and LO modes accurately, but also their oscillator strengths.

Next, we compare the calculated mode frequencies with the experimental values and previous calculations in Table I. We prefer to compare our calculations with the latest experimental data for the TO and LO modes by Clauws *et al.* [24] except for those modes that were not observed by them because they are too weak. Some of these were observed by Gilson *et al.* [22] as weak modes or by Abello *et al.* [25] in transmission. We should keep in mind that the B_{1u} and B_{2u} modes of Abello *et al.* [25] are interchanged from ours because of the choice of the y and z directions. However, we note that there is still some ambiguity in the assignment of the modes in that case because it is done on powders. For example, Abello *et al.* [25]

TABLE I. Infrared-active phonon frequencies: comparison of our calculated frequencies (cm^{-1}) with the experimental and previously reported work.

Mode	Expt.[a]	HGH[b]	error HGH	FHI[c]	error FHI	GGA[d]	error GGA
B_{1u}^{1T}	140[e]	136	−4	142	2	248	108
B_{1u}^{1L}	140	137	−3	143	3		
B_{1u}^{2T}	290[f]	291	1	295	5	329	39
B_{1u}^{2L}	290	292	2	297	7		
B_{1u}^{3T}	354[g]	358	4	338	−16	439	85
B_{1u}^{3L}	354	358	4	339	−15		
B_{1u}^{4T}	472	464	−8	477	5	481	9
B_{1u}^{4L}	492	481	−11	496	4		
B_{1u}^{5T}	570[h]	617	47	665	95	623	53
B_{1u}^{5L}	570	619	49	667	97		
B_{1u}^{6T}	974	1014	40	1014	40	1007	33
B_{1u}^{6L}	1040	1084	44	1084	44		
B_{2u}^{1T}	213	217	4	205	−8	254	41
B_{2u}^{1L}	226	227	1	208	−18		
B_{2u}^{2T}	285	285	0	271	−15	304	19
B_{2u}^{2L}	314	311	−3	302	−12		
B_{2u}^{3T}	506	496	−10	602	96	474	−32
B_{2u}^{3L}	844	825	−19	881	37		
B_{3u}^{1T}	72	72	0	74	2	72	0
B_{3u}^{1L}	78	73	−5	76	−2		
B_{3u}^{2T}	259	267	8	255	−4	327	68
B_{3u}^{2L}	267	268	1	257	−10		
B_{3u}^{3T}	302	339	37	362	60	347	45
B_{3u}^{3L}	389	384	−5	378	−12		
B_{3u}^{4T}	411	414	3	476	65	483	72
B_{3u}^{4L}	585	577	−8	619	34		
B_{3u}^{5T}	766	758	−8	849	84	768	2
B_{3u}^{5L}	965	934	−31	1010	45		
B_{3u}^{6T}	981	1011	30	1011	30	1006	25
B_{3u}^{6L}	987	1031	44	1023	36		
rms			22		43		55
max error			49		97		108

[a]Experimental data from Clauws and Vennik [24] from Kramers-Kronig analysis of reflectance, except as indicated.
[b]This work, LDA, Hartwigen-Goedecker-Hutter pseudopotential.
[c]This work, LDA Fritz-Haber pseudopotential.
[d]PW91-GGA with Troulier-Martins pseudopotentials by Brázdová *et al.* [27].
[e]From Gilson *et al.* [22], also observed by Abello *et al.* [25] at 144 cm^{-1}.
[f]From Abello *et al.* [25] powder transmission, ranging from 290–298 cm^{-1} in different hosts.
[g]From Gilson *et al.* [22], very weak.
[h]From Gilson *et al.* [22], also observed in transmission between 570 and 600 cm^{-1} by Abello *et al.* [25].

did not assign any observed peak to a B_{1u} mode near 350 cm^{-1} although Gilson *et al.* [22] did. The observed peak in the range 360–380 cm^{-1} which Abello *et al.* [25] assign to a B_{3u} mode could also contain the missing B_{1u} mode. On the other hand, a mode of B_{1u} symmetry near 290 was only reported by Abello *et al.* [25].

We compare our results also with previous calculations by Brázdová *et al.* [27]. They, however, do not report the LO modes, only the TO modes. The previous calculations by Zhou *et al.* [28] used exactly the same FHI pseudopotential and ABINIT code as ours and thus agree with ours to within 1–2 cm^{-1} and are thus not explicitly shown in the table. In the table, we include the errors from the selected experimental values. We can see that overall the root-mean-square error as well as the maximum error is lowest for the HGH pseudopotential. Closer inspection shows that the low-frequency modes tend to be already very close to experiment also in the FHI pseudopotential. The mode with the largest error turns out to be the B^5_{1u} mode which is rather uncertain experimentally because it is weak and was only reported in Gilson *et al.* [22]. In the transmission experiments on powders, it is found at 600 cm^{-1}, which is closer to our calculations.

We now discuss the cases with the remaining highest errors. By inspecting the nature of the modes involved, we find that all these have a strong bond-stretching character. To analyze the modes, we show first the symmetry pattern of the mode and second the relative magnitudes of the displacements on each atom of a given type. Here, we will just give a few examples. In Fig. 3(b), we labeled the vanadium atoms as V, the vanadyl oxygens as O_v, chain oxygens O_c, and bridge oxygens O_b. The different atoms of each type are given a number in Fig. 3(a), where the small spheres are V and the oxygens are labeled V_i, C_i, and B_i for vanadyl, chain, and bridge oxygen atoms, with i running from 1 to 4 or 1 to 2. The atom number given in the abscissa of Fig. 3(b) is simply the consecutive number of each atom, with the V first, followed by the vanadyl, chain, and bridge oxygens. The relative displacements of the atoms are shown in the ordinate of Fig. 3(b) with first the x then the z displacement in black and red, respectively. The same scheme is used for other similar figures. A full set for all modes is given in the Supplemental Material [40] that can be found online with the paper. As noted above, the modes fall in two categories, either they contain only y motion, or they contain x and z displacements. As an example, we show the highest B_{1u} mode in Fig. 3. We can see that it is almost completely a stretch mode of the vanadium vanadyl-oxygen bond.

Because LDA typically overestimates bonding, one may also expect that it will overestimate the corresponding phonon frequency. This is similar to the usual overestimate of the bulk modulus by LDA. On the other hand, one might expect that GGA would underestimate these phonon frequencies. We can see that for this high-frequency mode, the GGA results of Brázdová *et al.* [27] have a slightly smaller overestimate but they still overestimate the frequency. On the other hand, that calculation seems to overestimate also the low-frequency modes, so other errors must have occurred in this calculation either from the pseudopotential or other aspects of the calculation. The B^5_{1u} mode mentioned earlier can be seen to correspond to a stretch of the V-O_c bonds (Fig. 4). Although it has B_{1u} symmetry which is in principle infrared active for polarization $\mathbf{E}\|\mathbf{c}$, it has rather little dipole character in the z direction and therefore weak oscillator strength. The

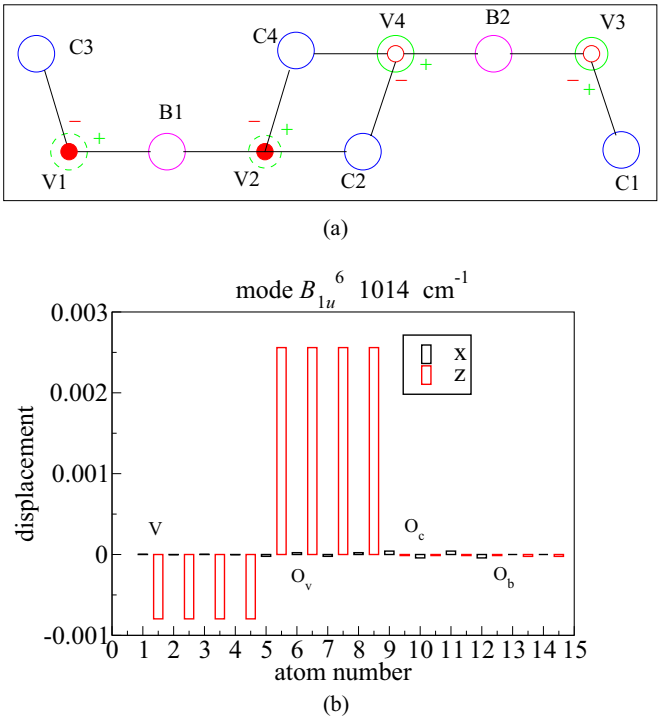

FIG. 3. (Color online) Displacement pattern of B^6_{1u} mode: (a) z motions are indicated by ± for each atom, (b) relative displacements in x (black) and z direction (red) for each atom as identified in (a).

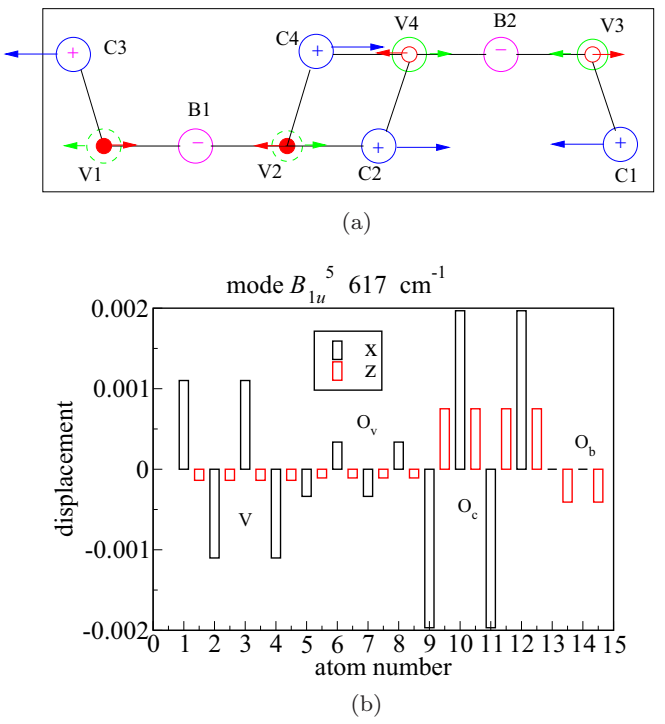

FIG. 4. (Color online) Displacement pattern of the B^5_{1u} mode. (a) x displacements are indicated by arrow, z motions by ±, (b) relative displacements of each atom as identified in (a).

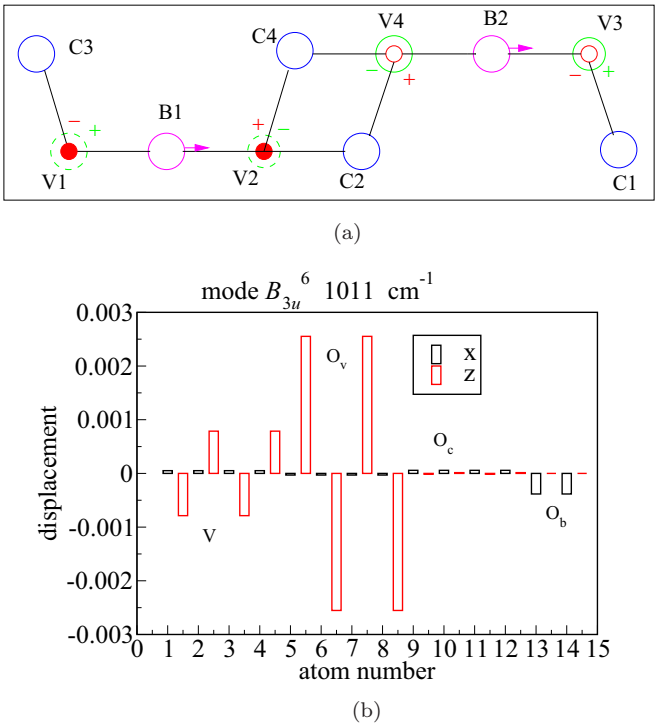

FIG. 5. (Color online) Displacement pattern for the B_{3u}^6 mode.

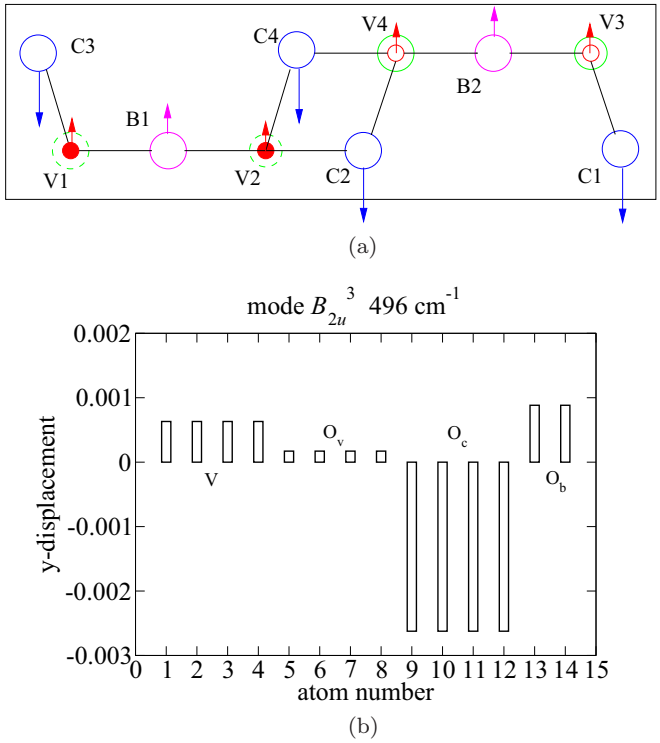

FIG. 6. (Color online) Displacement pattern for the B_{2u}^3 mode. This mode has only displacements in the y direction.

vanadium, vanadyl oxygen, and bridge oxygen are seen to move in the same direction in z and opposite to the chain oxygens, but the vanadium and the oxygen atoms of opposite charge moving in the same direction which leads to a weak dipole. The main motion is in the x direction.

Other modes that show large remaining overestimates are B_{3u}^3, B_{3u}^6, and B_{2u}^3. The B_{3u}^6 mode is again dominated by vanadium vanadyl-oxygen stretch, as is shown in Fig. 5. The only difference with B_{1u}^6 is that the V-O_v units on opposite sites of the bridge oxygen move opposite to each other. The B_{3u}^3 mode has a more complex character. The vanadium chain oxygen bond is stretched in the x direction but at the same time the vanadyl oxygen is moving opposite to the vanadium in the x direction and opposite to the chain oxygen in the z direction. The B_{2u}^3 mode is a mode purely in the y direction and involves a stretch of the chain oxygen along the direction of the chain (Fig. 6).

We conclude that most of the infrared modes are in good agreement with experiment both in frequency and in oscillator strength and the remaining discrepancy can be ascribed to the LDA overbonding.

C. Raman-active modes

The even modes with respect to the inversion labeled by subscript g are all Raman active and there are 21 in total. The A_{1g} modes are active for parallel incoming and scattered light polarizations, corresponding to a diagonal Raman tensor with different components xx, yy, and zz. Because of the layered nature of the crystal, it is easiest to perform measurements with the light incident normal to the c plane. With unpolarized light, one would then excite both xx and yy components of the tensor. The other modes correspond to crossed polarizations of incident and scattered light. B_{1g} corresponds to xy polarization and is also easily detected for light incident normal to the c plane. However, B_{2g} corresponds to xz and B_{3g} to yz components of the Raman tensor. As explained in Clauws *et al.* [26], these required measurements are on a thin cross section of a cleaved crystal. These measurements are more difficult to perform and a significant amount of modes from the other polarizations may leak through in these measurements. Thus, some of the peaks in the experimental spectra corresponding to the strong A_{1g} and B_{1g} symmetries are observed also in the geometry which should in principle select B_{2g} or B_{3g}. We have calculated the Raman tensor for all the Raman-active modes as explained in the method section. We should, however, remark that this method does not take into account any possible resonant effects because the susceptibility $\chi_{\alpha\beta}$ or rather its derivative versus atomic displacements is obtained in the limit that the frequency is far below the gap. The laser frequency used in the Raman study by Clauws *et al.* [26] had a frequency with energy $h\nu > E_g$ and thus some modes may have resonant effects.

We first compare the calculated frequencies with experiment and other calculations and then compare the actual Raman spectra. From Table II, we see that our calculated frequencies with the HGH pseudopotential for A_{1g} are pretty close to experiment except the highest frequency 1031 cm^{-1}. This mode is again overestimated with respect to the experimental value because it corresponds to a stretch mode of the V and vanadyl oxygen atoms O_v along the c axis, similar to what we discussed for the IR-active modes. For the B_{2g}^6 mode, the frequency 929 is underestimated compared to the experimental values 976 cm^{-1} of Abello *et al.* [25] and 965 cm^{-1} by Gilson *et al.* [22], which is not seen in the

TABLE II. Raman and A_{1u} modes: comparison of Raman frequencies (cm^{-1}) with the experimental and previously reported work.

Mode	HGH[a]	FHI[b]	Other[c]	Expt.[d]	Error[e]	Error[f]	Error[g]
A^2_{1u}	65	64	127	76[h]			
A^2_{1u}	275	254	297	263			
A^3_{1u}	492	601	468	533			
A^1_{1g}	104	108	137	107	−3	+1	30
A^2_{1g}	186	193	291	200	−14	−7	91
A^3_{1g}	303	295	383	310	−7	−15	73
A^4_{1g}	396	382	454	404	−8	−22	50
A^5_{1g}	467	528	484	483	−17	45	1
A^6_{1g}	518	542	539	528	−10	14	11
A^7_{1g}	1031	1029	1026	992	39	37	34
B^1_{1g}	147	167	169	147	0	20	22
B^2_{1g}	285	277	305	290	−5	−13	15
B^3_{1g}	693	772	676	702	−9	70	−26
B^1_{2g}	145	146	143	147	−2	−1	−4
B^2_{2g}	192	200	259	201	−9	−1	58
B^3_{2g}	309	299	385	315	−6	−16	70
B^4_{2g}	352	361	388	350 [25]	2	11	38
B^5_{2g}	482	528	500	507	−25	21	−7
B^6_{2g}	929	1010	936	963	−34	47	−27
B^7_{2g}	1029	1030	1024	992	37	38	32
B^1_{3g}	148	168	174	149	−1	17	25
B^2_{3g}	230	219	273	232	−2	−13	41
B^3_{3g}	285	279	311	291	−6	−12	20
B^4_{3g}	693	772	676	702	−9	70	−26
rms					17	31	41
max					39	70	91

[a]This work, HGH pseudopotential.
[b]This work, FHI pseudopotential.
[c]GGA calculation from Brázdová *et al.* [27].
[d]From Clauws *et al.* [26], except as noted.
[e]HGH result from experiment.
[f]FHI result from experiment.
[g]Brázdová *et al.* [27] from experiment.
[h]Calculated by Clauws *et al.* [26] using a force-field model fitted to IR and Raman observed modes.

Raman scattering experiment of Clauws *et al.* [26]. So, while this underestimate is unexpected, this mode is rather uncertain experimentally. These authors also do not list the lowest B_{2g}. A mode is visible in their spectrum but because it almost coincides with the strong B_{1g} mode they interpreted it as a mode leaking through from the wrong polarization. In their calculation with force constants fitted to the observed modes, they report this mode at 116 cm^{-1}. The B^7_{2g} mode at 1029 cm^{-1} is again overestimated by about 37 because it is a similar V-O_v stretch mode. However, this mode also has some stretch of the V-O_b bond in the x-direction character.

The overall error is seen to be lowest for the HGH pseudopotential. Although some modes have lower error for the FHI pseudopotential, the latter also shows some

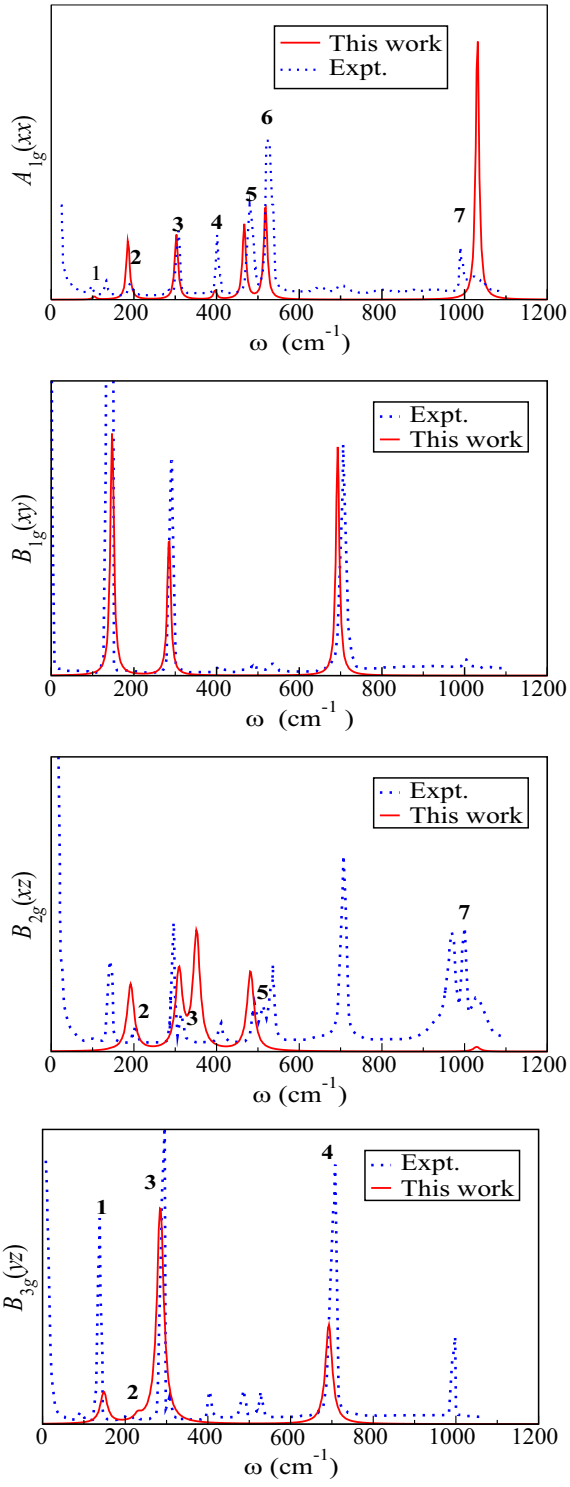

FIG. 7. (Color online) Intensity of Raman-active modes in arbitrary units as a function of frequency (in cm^{-1}) for bulk V_2O_5.

modes with significantly larger error. The GGA calculations by Brázdová *et al.* [27] again show overall an even larger discrepancy from experiment.

The Raman spectra were simulated using a fixed broadening parameter of 5 cm^{-1} for all the modes. In Fig. 7(a), we compare the measured intensity for the A^{xx}_{1g} Raman spectrum with our calculation. The other possible components A^{yy}_{1g}, A^{zz}_{1g} are

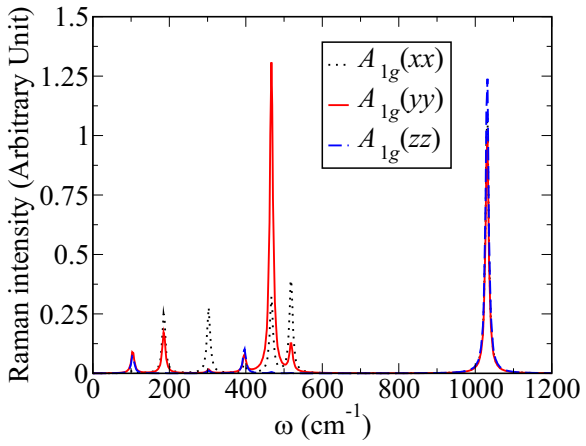

FIG. 8. (Color online) Comparison of Raman intensity of A_{1g} mode with different polarizations xx, yy, and zz.

shown in Fig. 8. To measure the yy component would only require a different polarization choice, while to measure the zz component would require us to use incident light on another surface than the natural cleavage plane. We can see that the tensor component significantly depends on the polarization although the mode frequencies stay the same.

The seven modes predicted by theory are all observed experimentally. However, the experiment shows an additional broader band at 1024 cm^{-1} and also an additional weak mode at about 150 cm^{-1} and broad weak peaks at about 650 and 700 cm^{-1}. The 150 and 700 cm^{-1} peaks may correspond to the strong B_{1g} modes which are leaking through. The high-frequency mode at 1024 cm^{-1} was discussed by Clauws *et al.* [26], but its origin remains unclear. One possibility is that this could be a LO-forbidden mode. The B_{1u}^{6L} mode lies at 1040 cm^{-1} according to the infrared data, so not too far from this band. Although such modes are nominally forbidden in first-order Raman, they can be activated by the Fröhlich interaction, in particular if the laser frequency is above the band gap and resonant effects are present [41,42]. Another possibility is that it corresponds to a disorder-induced Raman effect. This typically results in peaks corresponding to a high density of phonon states which tend to coincide with zone-boundary phonons. These may be expected to lie slightly lower than the LO mode at the zone center. The relative intensities of the calculated and measured xx component match well for the modes 3, 5, and 6 but the theory overestimates the intensity of the modes 2 and 7. As mentioned already, this could possibly be due to resonant Raman effects although it is by no means clear why these particular modes would be more susceptible to resonance effects.

The next following figures from Fig. 7(b) to bottom in Fig. 7(d) are B_{1g} (xy), B_{2g} (zx), and B_{3g} (yz) modes, respectively. We see that the three B_{1g} modes match very well in frequency and fairly well also in intensity. We also notice that the strong B_{1g}^1 and B_{1g}^3 modes leak through in the A_{1g} spectrum as well as the B_{2g} and B_{3g} spectra. We note that the B_{1g}^2 mode is very close to the B_{3g}^3 mode. The ABINIT code did not automatically distinguish these two modes because they are almost degenerate. By properly symmetrizing the two mode eigenvectors, we were able to extract the correctly symmetrized Raman tensors.

As mentioned before, the B_{2g} and B_{3g} modes are more difficult to observe experimentally because they require measurements on the thin cross sections of the crystals on a b plane and a plane. These spectra show significantly more breakthrough of the modes of the wrong polarization. The ones identified by the experimentalists as being of the expected symmetry character are labeled by numbers. For B_{2g} our calculated spectrum shows indeed modes near these frequencies, but the relative intensities differ and overall the calculated spectrum looks quite different from the measured one. For B_{3g}, the agreement is a little better, the modes 1, 3, and 4 match quite well in intensity as well as position, but still cross contamination with other modes is present in the experiment.

We note here that Zhou *et al.* [28] simulated the Raman spectrum for polycrystalline V_2O_5 using an appropriate averaging procedure of their calculated Raman intensities based on the same FHI pseudopotential as also used here and found overall fair agreement but did not get into details in the interpretation of the individual modes.

In summary, the Raman modes agree similarly well with experiment in frequency but the intensities agree less well than for the IR reflectivity measurements. This may have a few different origins. First, the experiments show significant cross leaking of one polarization to another. Second, the measurements were all done with a laser frequency above the gap of the semiconductor and may thus exhibit resonance effects not accounted for by our calculations. Third, the calculation of Raman intensities is more demanding as it is a third-order derivative and may thus suffer larger errors.

Finally, the three A_{1u} modes are silent but we may compare our calculated frequencies with those extracted from force-field calculations with parameters adjusted to the observed modes [26]. The agreement is fairly good as can be seen in Table II.

D. Comparison of phonons of bulk and monolayer(001)

Table III shows the comparison of phonon frequency for bulk and monolayer obtained by using two different pseudopotentials. From Table III, we see that a few low-frequency modes tend to red-shift while the highest frequency modes tend to blue-shift. The shifts are also shown in Fig. 9 for IR-active modes, Fig. 10 for A_{1g} and B_{1g}, and Fig. 11 for the B_{2g} and B_{3g} modes. Similar trends are seen with both pseudopotentials.

In these calculations, we kept the a and b lattice constants the same for monolayer as for bulk, but relaxed the internal positions for the monolayer.

The dielectric constants, both static and high frequency play possibly an important role in the long-range interactions. Therefore, before addressing the above-noted changes in the phonon frequencies, we first examine the dielectric constants. Strictly speaking, in a two-dimensional system, a wave-vector-independent dielectric constant is not well defined [43]. Instead, $\varepsilon(\mathbf{q}) = 1 + 2\pi\alpha_{2D}|\mathbf{q}|$. To extract the constant α_{2D} from supercell calculations, one needs to study the behavior as a function of spacing L between the layers and this should

TABLE III. Phonon frequencies in cm^{-1}: V_2O_5 bulk and monolayer(001).

	Bulk		Monolayer	
Mode	HGH	FHI	HGH	FHI
B^1_{1u}	136	142	95	92
B^2_{1u}	291	295	277	275
B^3_{1u}	358	338	368	352
B^4_{1u}	464	477	471	510
B^5_{1u}	617	665	606	651
B^6_{1u}	1014	1014	1104	1108
B^1_{2u}	217	205	216	204
B^2_{2u}	285	271	275	264
B^3_{2u}	495	602	510	600
B^1_{3u}	72	74	51	46
B^2_{3u}	267	255	241	228
B^3_{3u}	339	362	359	375
B^4_{3u}	414	476	422	487
B^5_{3u}	758	849	747	822
B^6_{3u}	1011	1011	1088	1096
A^1_{1g}	104	108	51	47
A^2_{1g}	185	193	170	171
A^3_{1g}	303	295	290	281
A^4_{1g}	396	381	407	394
A^5_{1g}	467	528	471	528
A^6_{1g}	518	542	522	546
A^7_{1g}	1031	1029	1103	1112
B^1_{1g}	147	167	136	148
B^2_{1g}	285	277	278	265
B^3_{1g}	693	772	701	769
B^1_{2g}	145	146	127	126
B^2_{2g}	192	200	178	179
B^3_{2g}	309	299	293	281
B^4_{2g}	352	361	345	353
B^5_{2g}	482	528	488	533
B^6_{2g}	929	1010	869	941
B^7_{2g}	1029	1030	1090	1100
B^1_{3g}	148	168	139	148
B^2_{3g}	230	219	237	231
B^3_{3g}	284	279	276	268
B^4_{3g}	693	772	701	770

vary as $1/L$. Here, we have just used one spacing L deemed large enough to be converged. Thus, our value for a monolayer should be understood as corresponding to a periodic array of monolayers spaced by a distance L. Using the bulk interplanar distance and the monolayer supercell interlayer distance, we find indeed that the $1/L$ behavior is approximately satisfied for the in-plane components of the dielectric constant and gives a $\alpha_{2D} \approx 1.6$ Å.

Table IV shows the changes in dielectric constants between bulk and monolayer. First, we note that the high-frequency dielectric tensor in-plane component ϵ_{xx}, ϵ_{yy} are reduced

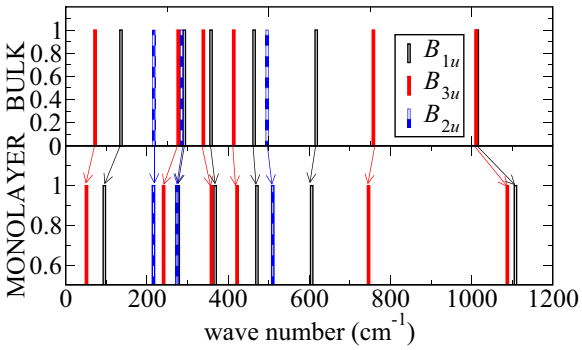

FIG. 9. (Color online) Comparison of B_{1u}, B_{2u}, and B_{3u} modes in bulk and monolayer calculated with HGH pseudopotential.

by about a factor 2 between bulk and monolayer. The ϵ_{zz} component is even more strongly reduced by a factor 2.7. The ratio of static to high-frequency dielectric constant coming from the Lyddane-Sachs-Teller relation is also slightly reduced from bulk to monolayer. This ratio is larger for in-plane than for out-of-plane modes and hence the anisotropy of the dielectric constants is stronger for the static values. This remains also true in the monolayer but overall, all the dielectric constants are significantly reduced in the monolayer compared to the bulk.

Next, we show the Born-effective charge tensor components for bulk and monolayer in Table V. These are calculated with the HGH pseudopotential. First, we note that the different oxygens have quite different Born-effective charges. For example, the vanadyl oxygen has a large Born-effective charge for coupling to electric fields in the z direction but a a small component in the x and y directions. On the other hand, the bridge oxygen has a large component in the x direction, while the chain oxygens have large x and y components. Clearly, this related to their coordination number and bonding to nearest neighbor V in those directions. We can see that some of the Born-effective charges are strongly reduced in the monolayer, while others are affected less. More specifically, the z components of all atoms are reduced by a factor 2.7–2.9, while the x and y components of the large Born charges are

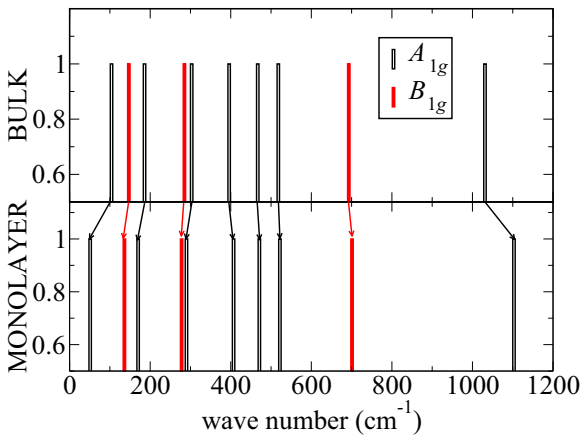

FIG. 10. (Color online) Comparison of A_{1g} and B_{1g} modes in bulk and monolayer calculated with HGH pseudopotential.

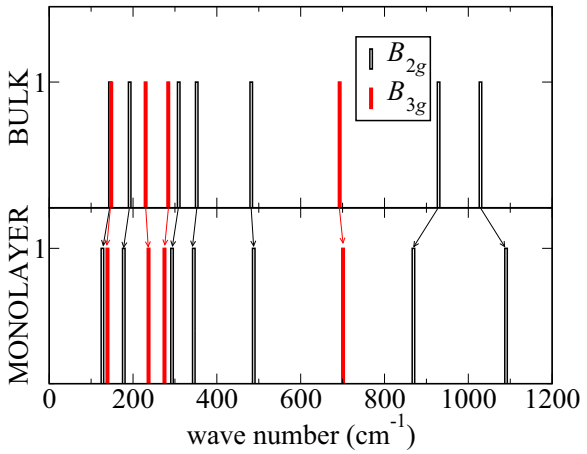

FIG. 11. (Color online) Comparison of B_{2g} and B_{3g} modes in bulk and monolayer calculated with HGH pseudopotential.

reduced much less, only about 10%. The y component of the bridge oxygen is even increased.

Finally, we show the interatomic force constants decomposed in their short- and long-range contributions for the most important near-neighbor pairs of atoms in Table VI for bulk and monolayer. All of these are calculated with the HGH potential.

Now, we are ready to discuss the shifts in phonon frequency between bulk and monolayer. Generally, one might think of two types of origin for these shifts. First, some interactions between atoms in different layers are removed in going to the monolayer. Generally, this would lead to a red-shift because removing springs decreases the stiffness of the system. It is easy to see this for a simple model of two weakly coupled oscillators. In the present case, we find that all interlayer force constants in the bulk are already of order $10^{-3}\ H/a_0^2$ [H is Hartree (27.2 eV) and a_0 is the Bohr radius $= 0.529$ Å] and thus they have little effect. In other words, the layers in bulk V_2O_5 are already weakly coupled. Second, the force constants in the layer may increase or decrease. This results from the change in balance of long- and short-range interactions as we will show in some detail below. The short-range interactions generally are expected not to change very much because the bond lengths do not change appreciably either. Nevertheless, some bonds get shortened and thus some short-range force constants might increase in the monolayer. More important is the long-range component of the force constants. These

TABLE IV. Dielectric constant of V_2O_5 bulk and monolayer(001).

		Bulk			Monolayer		
PSP	α	$\epsilon^0_{\alpha\alpha}$	$\epsilon^\infty_{\alpha\alpha}$	$\frac{\epsilon^0_{\alpha\alpha}}{\epsilon^\infty_{\alpha\alpha}}$	$\epsilon^0_{\alpha\alpha}$	$\epsilon^\infty_{\alpha\alpha}$	$\frac{\epsilon^0_{\alpha\alpha}}{\epsilon^\infty_{\alpha\alpha}}$
	x	17.18	6.12	2.81	6.49	2.92	2.22
FHI	y	15.08	5.49	2.75	6.00	2.70	2.22
	z	5.38	4.16	1.29	1.56	1.51	1.03
	x	26.22	6.54	4.00	8.53	2.97	2.87
HGH	y	22.03	6.08	3.62	7.75	2.75	2.82
	z	4.84	3.87	1.25	1.47	1.43	1.03

TABLE V. Born-effective charge ($Z_{I,\alpha\alpha}$), where I labels atom number (species) and $\alpha\alpha$ for xx, yy, or zz diagonal components.

V_2O_5	Atom	$Z_{I,xx}$	$Z_{I,yy}$	$Z_{I,zz}$
	V	6.700	6.280	3.325
	O_v	−0.557	−0.568	−2.225
Bulk	O_c	−2.588	−5.213	−0.761
	O_b	−7.109	−0.997	−0.679
	V	6.131	5.826	1.208
Monolayer	O_v	−0.378	−0.417	−0.820
	O_c	−2.543	−4.879	−0.263
	O_b	−6.418	−1.059	−0.250

result from the dipole interactions and are affected by both the changes in dielectric constant and the Born-effective charges.

We now examine first the origin of the blue-shift of the high-frequency modes B^6_{1u}, B^6_{3u}, A^7_{1g}, B^7_{2g}. All these modes are essentially stretch modes of the vanadium to vanadyl-oxygen bond. They differ mostly just by the relative phases of the displacements on the four different V-O_v pairs in the unit cell. However, some of these modes also have a little bit of V-O_b stretch component. The B^6_{1u} is the most pure V-O_v stretch mode and should thus be given approximately by $\omega = \sqrt{K/\mu}$ with K the relevant force constant and μ the reduced mass. Since it involves only motion in the z direction, we can focus on the V-O_v z component of the force constant. We can see from Table VI that the total force constant is indeed increased in magnitude in the monolayer compared to the bulk by about 12%. Thus, one expects the frequency to be increased by about 6%. In fact, all four modes considered in this paragraph are blue-shifted by about 5.9%–8.8%. Next, we can see that short-range component of the force constant and the long-range component are opposite to each other and that the short-range component stays more or less the same in bulk and monolayer, which is consistent with the negligible change in bond length. However, the long-range component is significantly reduced in magnitude. The longest-range force constant contribution is the dipole-dipole interaction [44] which is given by

$$K_{I\alpha,J\beta} = \frac{Z_{I\alpha}Z_{J\beta}}{\sqrt{\epsilon_{xx}\epsilon_{yy}\epsilon_{zz}}}\left(\frac{\epsilon^{-1}_{\alpha\beta}\delta_{\alpha\beta}}{D^3} - 3\frac{\epsilon^{-1}_{\alpha\alpha}\epsilon^{-1}_{\beta\beta}d_\alpha d_\beta}{D^5}\right), \quad (3)$$

where we have used that the crystal is orthorhombic and thus has diagonal Z and ϵ tensors. Here, summation over repeated indices is assumed and $D = \sqrt{\epsilon^{-1}_{\alpha\alpha}d^2_\alpha}$ and $\mathbf{d} = \mathbf{d}_{IJ}$ is the vector joining atom I with atom J. In our case, we need only the zz component of the force constant, so $\alpha = \beta = z$ and the relevant long-range force constant is reduced to

$$K_{Vz,O_{vz}} = -2\frac{Z_{Vz}Z_{Ovz}}{\sqrt{\epsilon_{xx}\epsilon_{yy}}d^3}. \quad (4)$$

Now, we can see from Table V that the Born-effective charges are reduced by a factor 2.7 each and the dielectric constants are each reduced by a factor 2. Thus, the long-range force constant is expected to be reduced by a factor 3.7. In fact, the bulk value is 0.088 H/a_0^2, while the monolayer value is 0.027

TABLE VI. Interatomic force constants ($K_{I\alpha,J\alpha}$), where I/J label the atom and α labels the Cartesian direction. The V-V pair is a nearest-neighbor pair while V-O_b-V means the two V joined by a O_b in-between. The atoms labeled by a prime lie in the adjacent plane. The forces are decomposed in their long- and short-range contributions, the three numbers correspond to (x,y,z) components of the force constant. The bond length (in Å) between the pairs is given in the last column. All force constants are in hartree/Bohr radius^2.

V_2O_5	Spring	$K_{I\alpha,J\alpha}$ (Total)	$K_{I\alpha,J\alpha}$ (Long range)	$K_{I\alpha,J\alpha}$ (Short range)	Bond length
	V-O_b-V	−0.0588, 0.0248, 0.0027	−0.0674, 0.0318, 0.0143	0.0085,−0.0070,−0.0116	3.4388
	V-V	−0.0267, 0.0162, 0.0011	−0.0218, 0.0005, 0.0121	−0.0049, 0.0157,−0.0110	3.0789
Bulk	V-O_v	−0.0383,−0.0306,−0.4786	−0.0132,−0.0135, 0.0878	−0.0252,−0.0171,−0.5665	1.5785
	V-O_{c1}	−0.0178,−0.0604,−0.0281	−0.0597, 0.2306,−0.0099	0.0419,−0.2910,−0.0182	1.8732
	V-O_{c2}	−0.0275,−0.0542,−0.0197	0.1093,−0.1236,−0.0028	−0.1368, 0.0694,−0.0169	2.0060
	V-O_b	−0.1190,−0.0104,−0.0323	0.4228,−0.0347,−0.0122	−0.5418, 0.0243,−0.0201	1.7727
	O_{c1}-O_{c2}	−0.0054,−0.0274, 0.0061	−0.0036,−0.0477, 0.0015	−0.0018, 0.0204, 0.0046	2.3635
	O_v-$O_{v'}$	−0.0013,−0.0006, 0.0001	−0.0003,−0.0001, 0.0088	−0.0010,−0.0006,−0.0087	2.9427
	V-$O_{v'}$	−0.0024,−0.0025,−0.0007	−0.0024,−0.0025,−0.0007	0.0000, 0.0000, 0.0000	2.7880
	O_v-$O_{b'}$	0.0014, 0.0004,−0.0021	0.0014, 0.0004,−0.0021	0.0000, 0.0000, 0.0000	2.9126
	V-O_b-V	−0.0323, 0.0529, 0.0048	−0.1413, 0.0672, 0.0061	0.1091,−0.0143,−0.0013	3.4051
	V-V	−0.0164, 0.0297, 0.0020	−0.0487, 0.0047, 0.0053	0.0323, 0.0250,−0.0033	3.0959
Monolayer	V-O_v	−0.0406,−0.0368,−0.5355	−0.0152,−0.0171, 0.0266	−0.0254,−0.0197,−0.5621	1.5609
	V-O_{c1}	−0.0207,−0.0850,−0.0344	−0.1256, 0.4415, 0.0000	0.1049,−0.5265,−0.0344	1.8821
	V-O_{c2}	−0.0323,−0.1107,−0.0261	0.2380,−0.2498, 0.0014	−0.2704, 0.1391,−0.0275	2.0110
	V-O_b	−0.1101,−0.0244,−0.0450	0.6546,−0.0742,−0.0019	−0.7646, 0.0498,−0.0431	1.7844
	O_{c1}-O_{c2}	−0.0055,−0.0137, 0.0076	−0.0085,−0.0998, 0.0000	0.0031, 0.0861, 0.0076	2.3640
	O_v-$O_{v'}$	0.0000, 0.0000, 0.0000	0.0000, 0.0000, 0.0000	0.0000, 0.0000, 0.0000	
	V-$O_{v'}$	0.0000, 0.0000, 0.0000	0.0000, 0.0000, 0.0000	0.0000, 0.0000, 0.0000	
	O_v-$O_{b'}$	0.0000, 0.0000, 0.0000	0.0000, 0.0000, 0.0000	0.0000, 0.0000, 0.0000	

H/a_0^2, so indeed the monolayer value is reduced by a factor 3.3. Now, the long-range part 0.087 H/a_0^2 is only about 15% of the short-range part (0.566 H/a_0^2) and thus the reduction of the long-range part has only about a 12% increase effect on the total force constant consistent with the first-principles results. This example shows that the blue-shift of these modes can be accounted for semiquantitatively in terms of the reduction in long-range force constant and the delicate balance of the long- and short-range force constants. The reduction of the long-range force constant in turn is due to the dominance of the reduction in the Born-effective charges compensated by a reduction in dielectric constants, which by itself would have increased the force constant.

Next, we consider the red-shift of the A_{1g}^1 mode. The displacement pattern of this mode is shown in Fig. 12. We can see that in this mode the vanadium and its vanadyl-oxygen move together in both the x and z directions. They both move toward the bridge oxygen, which moves up or down in the two halves of the cell. In fact, we can see that entire chains (along y) on either side of a bridge oxygen move toward the bridge and move up and down with the bridge oxygen. However, the two chains in one double chain related to each other by the inversion center move opposite to each other. By inspecting the motion in this structure, one expects that the V_x-V_x force constants between V in the same double chain, the V-O_b-V connected by a bridge oxygen, and the V-O_b force constants could play a role in the effective force constant of this mode. Inspection of the force-constant table shows that all three of these force constants are in fact reduced in the monolayer. Again, there is a subtle interplay of changes in long- and short-range components of the force constants. For example, for the V-V interaction, the short-range force constant increases and changes sign so as to oppose the long-range part in the monolayer whereas they reinforced each other in the bulk. In these x-direction interactions, the long-range force constant now has a factor $\sqrt{\epsilon_{yy}\epsilon_{zz}}$. This increases the long-range force constant almost by a factor 2 because the x component of the Born-effective charge on V is only slightly reduced. The same applies to the V-O_b-V interaction, which has a very small short-range component in the bulk, which is increased in the monolayer. Again, in the end the net force constant in the x direction is reduced. The B_{1u}^1 mode has a similar motion of chains moving in the x direction relative to the bridge oxygens and thus a similar analysis applies and explains the strong red-shift of this mode. It is also clear that both these modes are low-frequency modes because many atoms move together, so the effective total mass in the oscillator is large.

The B_{2g}^6, although a high-frequency mode, also shows a red-shift. Its vibrational pattern is shown in Fig. 13. We can see that in this mode there is a strong x motion of the bridge oxygen atoms opposite to each other. The V atoms move far less and thus the strongest force constant affecting this mode is the V-O_b bond-stretch mode. We can see that this force constant is reduced by about 8%. This corresponds to a 4% reduction in frequency. The actual red-shift is about 6% and is larger because the mode is not purely this stretch mode.

While our discussion of the modes may be somewhat oversimplified because most modes are rather complex motions, they provide at least some insight into the origin of the red- and blue-shifts. They result from the changes in force

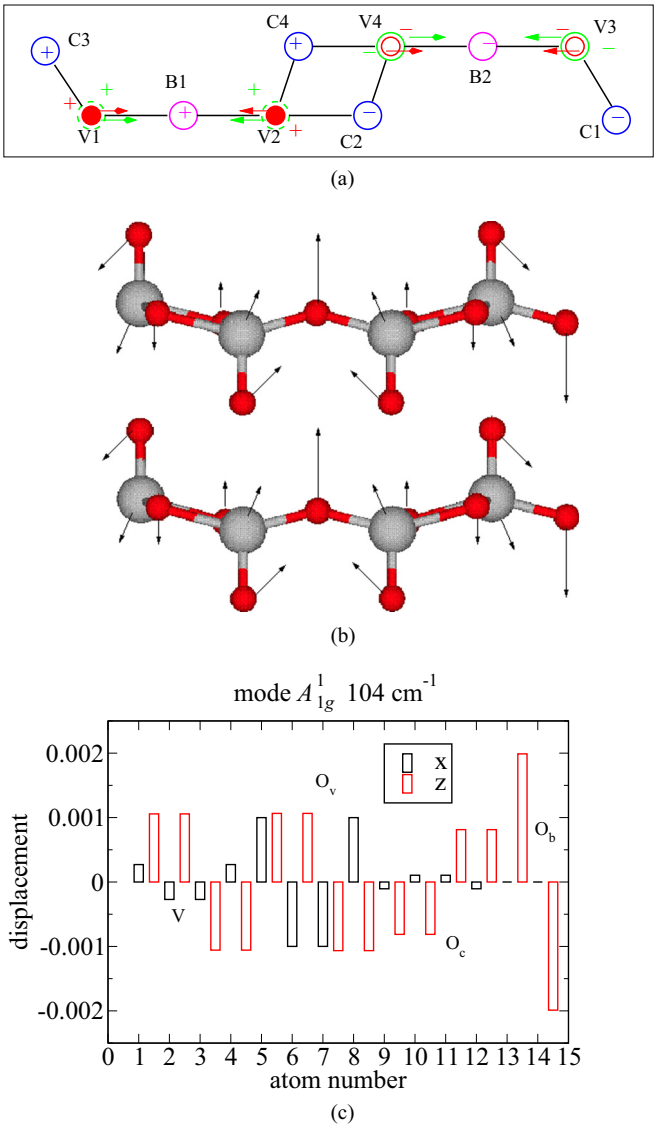

FIG. 12. (Color online) Displacement pattern for the A^1_{1g} mode.

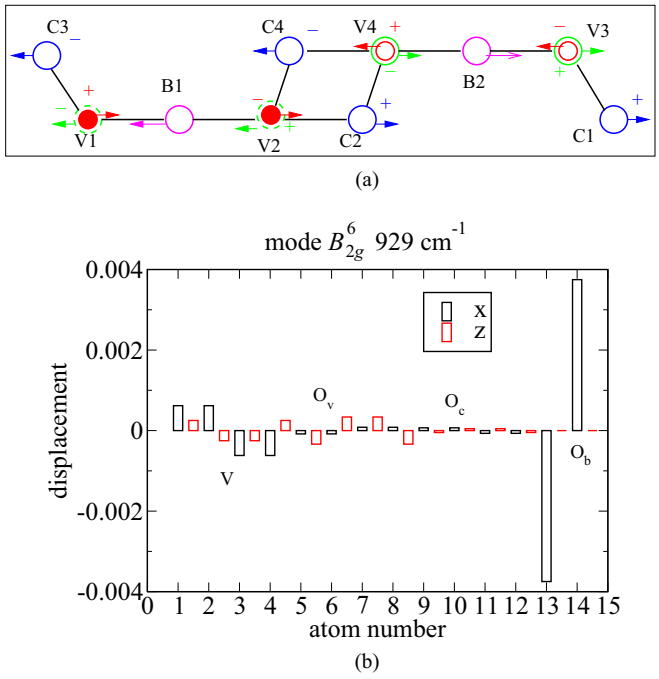

FIG. 13. (Color online) Displacement pattern for the B^6_{2g} mode.

constants in the layer rather than from the removal of interlayer interactions.

It is perhaps useful to compare the situation with MoS_2 monolayers for which the changes in frequency were recently discussed in two papers [30,45]. First, in that case, the observed changes in frequency are significantly smaller. Second, in that case, the in-plane mode E_{2g} was found to blue-shift while the out-of plane mode A_{1g} was found to red-shift. In contrast, we can see here that the strongest blue-shift in V_2O_5 occurs for out-of-plane motions. In the case of MoS_2, the long-range interactions were found to significantly increase because of the reduction of dielectric screening, while the Born-effective charges stayed the same. Here, we find instead a decrease of the Born-effective charges to play an important role in addition to the reduction of the dielectric screening. In spite of decreasing the long-range force constants, they lead on balance to an increased force constant in the monolayer because of their counteracting effect against the short-range forces for the vanadium-vanadyl stretch modes. The removal of interlayer interactions played an important role for MoS_2 in explaining the red-shift, while here it does not. While a similar analysis of long- and short-range force constants turned out to be helpful to provide some understanding, the conclusions about the final behavior of the frequencies from bulk to monolayer are quite different. The much more complex structure also means that the modes are no longer as easy to describe in terms of just a single or a few force constants. In summary, the trend of phonon frequency changes between bulk and monolayer is by no means universal.

V. CONCLUSION

We studied the normal modes of vibration in V_2O_5 for two different pseudopotentials using the density functional perturbation (DFPT) method within the local density approximation. We noticed that the Gaussian relativistic HGH pseudopotential gave better results compared to the FHI pseudopotential for bulk. We presented a more detailed analysis of the comparison of the calculated with the experimental results than in previous literature. Our results for the infrared reflectivity obtained with the HGH pseudopotential are in excellent agreement with the experimental results both in terms of frequencies and oscillator strengths. We found that our calculated Raman intensities are also in fair agreement with experimental results although the relative intensities show somewhat larger discrepancies. The remaining overestimates of some of the mode frequencies were ascribed to the typical overbinding of LDA and occur for modes corresponding primarily to a stretch mode.

Next, we studied the changes in frequencies between bulk and monolayer. An analysis of the force constants was used to explain the blue-shift of the high-frequency modes and the

red-shift of some of the lower-frequency modes. It is found to result from changes in the force constants within a layer, resulting from a delicate balance of long- and short-range contributions to the force constants, rather than from the cutting of interlayer bonds. The reduction of long-range dipolar interaction contributions to the force constants was in this case found to be reduced in monolayer from bulk due a reduction of the Born-effective charges, partially compensated by a reduced screening.

ACKNOWLEDGMENTS

The calculations made use of the High Performance Computing Resource in the Core Facility for Advanced Research Computing at Case Western Reserve University. The work was supported by the Air Force Office of Scientific Research under Grant No. FA9550-12-1-0441. The portion of the work on infrared and Raman spectroscopy was supported by the U.S. Department of Energy, Basic Energy Sciences, under Award No. ER 46874 SC0008933.

[1] H. J. Zeiger, Phys. Rev. B **11**, 5132 (1975).
[2] D. Grieger, C. Piefke, O. E. Peil, and F. Lechermann, Phys. Rev. B **86**, 155121 (2012).
[3] F. J. Morin, Phys. Rev. Lett. **3**, 34 (1959).
[4] V. Eyert, Phys. Rev. Lett. **107**, 016401 (2011).
[5] L. Fiermans, P. Clauws, W. Lambrecht, L. Vandenbroucke, and J. Vennik, Phys. Status Solidi A **59**, 485 (1980).
[6] S. Beke, Thin Solid Films **519**, 1761 (2011).
[7] R.-P. Blum, H. Niehus, C. Hucho, R. Fortrie, M. V. Ganduglia-Pirovano, J. Sauer, S. Shaikhutdinov, and H.-J. Freund, Phys. Rev. Lett. **99**, 226103 (2007).
[8] D. W. Bullett, J. Phys. C: Solid State Phys. **13**, L595 (1980).
[9] W. Lambrecht, B. Djafari-Rouahni, and J. Vennik, J. Phys. C: Solid State Phys. **14**, 4785 (1981).
[10] S. Das, X. Ma, X. Zong, A. Niazi, and D. C. Johnston, Phys. Rev. B **74**, 184417 (2006).
[11] V. Petkov, P. Y. Zavalij, S. Lutta, M. S. Whittingham, V. Parvanov, and S. Shastri, Phys. Rev. B **69**, 085410 (2004).
[12] G.-m. Zhu, Z.-b. Qu, G.-l. Zhuang, Q. Xie, Q.-q. Meng, and J.-g. Wang, J. Phys. Chem. C **115**, 14806 (2011).
[13] J. Bailey, G. Pozarnsky, and M. Mecartney, J. Mater. Res. **7**, 2530 (1992).
[14] G. T. Kim, J. Muster, V. Krstic, J. G. Park, Y. W. Park, S. Roth, and M. Burghard, Appl. Phys. Lett. **76**, 1875 (2000).
[15] J. Muster, G. T. Kim, V. Krsti, J. G. Park, Y. W. Park, S. Roth, and M. Burghard, Adv. Mater. **12**, 420 (2000).
[16] A. D. Raj, P. S. Kumar, Q. Yang, and D. Mangalaraj, Physica E (Amsterdam) **44**, 1490 (2012).
[17] A. Talledo and C. G. Granqvist, J. Appl. Phys. **77**, 4655 (1995).
[18] G. Gu, M. Schmid, P.-W. Chiu, A. Minett, J. Fraysse, G.-T. Kim, S. Roth, M. Kozlov, E. M. Noz *et al.*, Nat. Mater. **2**, 316 (2003).
[19] J. Livage, Chem. Mater. **3**, 578 (1991).
[20] G. Micocci, A. Serra, A. Tepore, S. Capone, R. Rella, and P. Siciliano, J. Vac. Sci. Technol. A **15**, 34 (1997).
[21] Y. Wang, K. Takahashi, K. Lee, and G. Cao, Adv. Funct. Mater. **16**, 1133 (2006).
[22] T. R. Gilson, O. F. Bizri, and N. Cheetham, J. Chem. Soc. Dalton Trans. **3**, 291 (1973).
[23] B. Bootz, H. Finkenrath, G. Franz, and N. Uhle, Solid State Commun. **13**, 1477 (1973).
[24] P. Clauws and J. Vennik, Phys. Status Solidi B **76**, 707 (1976).
[25] L. Abello, E. Husson, Y. Repelin, and G. Lucazeau, Spectrochim. Acta, Part A **39**, 641 (1983).
[26] P. Clauws, J. Broeckx, and J. Vennik, Phys. Status Solidi B **131**, 459 (1985).
[27] V. Brázdová, M. V. Ganduglia-Pirovano, and J. Sauer, Phys. Rev. B **69**, 165420 (2004).
[28] B. Zhou and D. He, J. Raman Spectrosc. **39**, 1475 (2008).
[29] H. Poelman, L. Fiermans, J. Vennik, and G. Dalmai, Solid State Commun. **84**, 811 (1992).
[30] A. Molina-Sánchez and L. Wirtz, Phys. Rev. B **84**, 155413 (2011).
[31] R. Enjalbert and J. Galy, Acta Crystallogr., Sect. C: Cryst. Struct. Commun. **42**, 1467 (1986).
[32] X. Gonze, J. M. Beuken, R. Caracas, F. Detraux, M. Fuchs, G. M. Rignanese, L. Sindic, M. Verstraete, G. Zerah, F. Jollet *et al.*, Comput. Mater. Sci. **25**, 478 (2002).
[33] X. Gonze, B. Amadon, P. M. Anglade, J. M. Beuken, F. Bottin, P. Boulanger, F. Bruneval, D. Caliste, R. Caracas, M. Côté *et al.*, Comput. Phys. Commun. **180**, 2582 (2009).
[34] M. C. Payne, M. P. Teter, D. C. Allan, T. A. Arias, and J. D. Joannopoulos, Rev. Mod. Phys. **64**, 1045 (1992).
[35] X. Gonze, D. C. Allan, and M. P. Teter, Phys. Rev. Lett. **68**, 3603 (1992).
[36] X. Gonze and J.-P. Vigneron, Phys. Rev. B **39**, 13120 (1989).
[37] J. P. Perdew and Y. Wang, Phys. Rev. B **45**, 13244 (1992).
[38] C. Hartwigsen, S. Goedecker, and J. Hutter, Phys. Rev. B **58**, 3641 (1998).
[39] H. B. Schlegel, J. Comput. Chem. **3**, 214 (1982).
[40] See Supplemental Material at http://link.aps.org/supplemental/10.1103/PhysRevB.89.045109 for a full set of displacement patterns for all modes.
[41] R. M. Martin, Phys. Rev. B **4**, 3676 (1971).
[42] P. F. Williams and S. P. S. Porto, Phys. Rev. B **8**, 1782 (1973).
[43] P. Cudazzo, I. V. Tokatly, and A. Rubio, Phys. Rev. B **84**, 085406 (2011).
[44] X. Gonze and C. Lee, Phys. Rev. B **55**, 10355 (1997).
[45] X. Luo, Y. Zhao, J. Zhang, Q. Xiong, and S. Y. Quek, Phys. Rev. B **88**, 075320 (2013).